Structural changes of tempered martensitic 9%Cr–2%W–3%Co steel during creep at 650 °C

N. Dudova[a,*], A. Plotnikova[a], D. Molodov[b], A. Belyakov[a], R. Kaibyshev[a]

[a] Belgorod State University, Belgorod 308015, Russia
[b] Institute of Physical Metallurgy and Metal Physics, RWTH Aachen University, 52056 Aachen, Germany

A B S T R A C T

The structural changes in tempered martensitic 9Cr–2W–3Co (wt%) steel during creep tests at 650 °C were studied. The starting material was a solution treated at 1050 °C and subsequently tempered at 750 °C. The tempered martensite substructure consisted of a mixture of crystallites with a lath-type morphology and equiaxed subgrains. The tempering resulted in the precipitation of numerous second phase particles. MX-type precipitates were homogeneously distributed within the ferritic matrix, whereas $M_{23}C_6$-type carbides were located on boundaries. Under creep conditions, Laves phase particles also precipitated at (sub)grain/lath boundaries. Laths and subgrains tended to coarsen during creep. It was shown that $M_{23}C_6$-type carbides played a major role in the stabilization of the tempered martensite lath structure by exerting a large pinning pressure. The transition to tertiary creep correlated with a coarsening of the carbides and a detachment of lath and subgrain boundaries from the chains of these carbides that led to a decreased pinning force from $M_{23}C_6$ carbides.

Keywords:
Martensite
Steel
Phase transformation
Creep
Precipitation
Coarsening

1. Introduction

High chromium martensitic steels are advanced engineering materials used to construct various components in novel fossil power plants [1,2]. The superior creep resistance of these steels is attributed to a tempered martensite lath structure (TMLS), which is stabilized by a dispersion of nanoscale particles [3–7]. MX-type carbides precipitate homogeneously within a martensitic matrix, while $M_{23}C_6$-type carbides precipitate on the boundaries of laths, blocks, packet and prior austenite grains (PAGs) during tempering. In addition, Laves phase particles precipitate at the boundaries during creep [7–9]. Lath boundaries have low mobility and hinder dislocation movement at high temperatures [4]. It was recently demonstrated [10–12] that a submicrometer-scale lath thickness and a high dislocation density are key contributors to the high creep strength of steels with TMLS; carbide and Laves phase particles play an important role in providing creep resistance. These particles contribute to the creep strength of steels with TMLS by interrupting knitting reactions between free dislocations and low-angle grain boundaries [10] and by exerting Zener forces on high-angle and low-angle boundaries that stabilize the TMLS under creep conditions. The particles also prevent the occurrence of dynamic recrystallization and dynamic polygonization. The stability of the TMLS is a key contributing factor to the creep resistance of martensitic steels [5,10,12–17].

The numerous precipitates exert a high Zener pinning pressure on various boundaries [7], providing the stability of the TMLS. However, at elevated temperatures, the precipitates coarsen with time by Ostwald ripening that diminishes both the dispersion strengthening and the Zener pinning pressure. As a result, the TMLS becomes unstable [4–7,10,12–17]; laths tend to transform into subgrains, which grow and deteriorate the creep resistance. In commercial martensitic steels, subgrain coarsening eventually leads to a degradation of the creep resistance [3–7,12–17], causing an increase in the creep rate and a transition from steady-state creep to tertiary creep, thereby limiting the lifetime of these steels under creep conditions. A high resistance of dispersed particles against coarsening during prolonged exposure to high temperatures is necessary to achieve high creep strength. However, the exact role of the aforementioned particles and their contribution to the creep strength of steels with TMLS are not fully understood because only a limited number of works [5,10,12–17] have examined the microstructural evolution.

It was assumed that a dispersion of M(C, N) carbonitrides, which precipitate mainly within the matrix and less frequently on lath boundaries, contributes greatly in stabilizing the TMLS [1,3,18–20]. The high resistance of M(C, N) carbonitrides to coarsening during creep is provided by two-phase separation on V-rich and Nb-rich precipitates [21,22]. This separation is in thermodynamic equilibrium and strongly hinders the coagulation of M(C, N)

* Corresponding author. Tel.: +7 4722 585417; fax: +7 4722 585417.
E-mail address: dudova@bsu.edu.ru (N. Dudova).

carbonitrides under creep conditions [7,22]. In contrast to MX precipitates, $M_{23}C_6$ carbides are easily susceptible to growth under creep conditions [12,14,16,18,22,23]. As a result, the contribution of these carbides to the creep resistance of martensitic steels was considered to be minor. On the other hand, recent works suggested that $M_{23}C_6$ carbides play a more important role than MX precipitates in the control of subgrain coarsening and the consequent long-range creep strength [12,15]. Thus, the primary aim of the present study was to gain a deeper understanding of the role of different second phase particles in stabilizing the TMLS during creep. These data are important in establishing an alloying concept for further improving the creep resistance of high chromium martensitic steels through the modification of their chemical composition.

Alloying with cobalt was shown to have a beneficial effect on the creep properties of martensitic steels [7,22–27]. It is commonly believed that cobalt slows down diffusion within the ferritic matrix, leading to a significant decrease in the rate of Ostwald ripening of $M_{23}C_6$ carbides and therefore promoting the stability of the TMLS. However, the structural changes in cobalt containing 9%Cr martensitic steels during creep have not been studied in great detail. Thus, the second aim of this work was to examine the microstructure evolution in a 3%Co modified P92-type steel during creep. The microstructural data obtained in investigations of P92 steels with and without cobalt [12] are analyzed with respect to cobalt's role in enhancing the creep resistance of 9%Cr martensitic steels.

2. Experimental procedure

A Co-modified P92-type steel, Fe–0.1C–0.3Si–0.5Mn–9.0Cr–0.1Ni–0.6Mo–1.8W–0.2V–0.06Nb–0.05N–3.0Co–0.005B (all in wt%), was cast and hot forged in the Central Research Institute for Machine-Building Technology, Moscow, Russia. The steel was solution treated at 1050 °C, cooled by air, and subsequently tempered at 750 °C for 3 h. Flat specimens with a gauge length of 25 mm and a cross section of 7 mm × 3 mm were subjected to creep tests to various strains and until rupture to examine the microstructure evolution. The creep tests were carried out at 650 °C under initial stresses of 140–200 MPa in steps of 20 MPa.

The structural investigations were carried out on the tempered sample and on the longitudinal section of the crept specimens using the Z-contrast technique [22,27] with a Quanta 600FEG scanning electron microscope equipped with an electron back scatter diffraction (EBSD) pattern analyzer incorporating an orientation imaging microscopy (OIM) system and a JEM-2100 transmission electron microscope (TEM) with an INCA energy dispersive X-ray spectroscope. The grip and neck portions of the crept microstructures in the fractured samples were studied separately. The OIM images were subjected to a cleanup procedure, setting the minimal confidence index to 0.1. TEM foils were prepared by double jet electro-polishing using a solution of 10% perchloric acid in glacial acetic acid. The grain sizes (D_{HAB}) were measured on OIM images as the average spacing between high-angle boundaries with misorientations above 15°. The lath/subgrain sizes were evaluated on TEM micrographs by the linear intercept method including all clearly visible (sub)boundaries. The dislocation densities were estimated by counting the individual dislocations in the grain/subgrain interiors per unit area on at least six arbitrarily selected typical TEM images for each data point. The density of particles located at (sub)grain/lath boundaries was determined as the number of particles per unit boundary length. The volume fractions of the precipitated phases were calculated by the Thermo-Calc software using the TCFE4 database. The coarsening of a $M_{23}C_6$ particle in model alloys was calculated using the Dictra software version 26.

3. Results

3.1. Tempered microstructure

Typical images of the TMLS are shown in Fig. 1. The size of the PAGs is approximately 10 μm (Fig. 1a and Table 1). The mean spacing of high-angle boundaries is 3.4 μm (Table 1). The TMLS is characterized by the presence of two substructural components. Some portions of the structure are filled with typical martensite laths [28] with a transverse size of 380 nm, while other portions are composed of essentially equiaxed subgrains that have an average size of 500 nm (Fig. 1c). The TMLS is characterized by a rather high dislocation density of 2×10^{14} m^{-2}; lattice dislocations were found within the interiors of both laths and subgrains. It is worth noting that the formation of equiaxed subgrains under tempering at a relatively low temperature is rarely observed in high chromium martensitic heat resistant steels [4]. Nevertheless, this microstructure is commonly interpreted as a TMLS [28].

The tempering resulted in the formation of numerous $M_{23}C_6$-type particles on the boundaries of PAGs, packets, blocks, and laths/subgrains (Fig. 1b). The mean size of these precipitates is approximately 90 nm, and their volume fraction calculated using Thermo-Calc software is approximately 0.02. In addition to such relatively large particles, the TMLS involves fine MX-type carbonitrides including VC and NbC particles with sizes of 20 nm and 40 nm, respectively; M(C, N) carbonitrides are homogeneously distributed within the ferritic matrix (Fig. 1d and e). The two aforementioned types of carbonitrides can be easily distinguished by their morphology because V-rich M(C, N) particles primarily have a "wing" shape [19].

3.2. Creep behavior

Fig. 2a displays a series of creep rate vs. creep time curves obtained during tests at 650 °C under different nominal stresses.

Table 1
Evolution of structural parameters during creep test.

	Strain (%)					
	0	1	4	5.5	12	
					Neck	Grip
Time (h)	0	108	1165	1482	1828	1828
D_{HAB} (μm)	3.4	3.5	3.5	3.6	3.6	3.4
D lath (μm)	0.38	0.43	0.54	0.75	0.93	0.38
D subgrain (μm)	0.5	0.55	0.7	1.45	1.45	1.2
Dislocation density (m^{-2})	2×10^{14}	1.5×10^{14}	1.2×10^{14}	0.7×10^{14}	0.2×10^{14}	1.8×10^{14}
Mean size of $M_{23}C_6$[a] (nm)	90	120	120	150	185	150
Mean size of VX[a] (nm)	20	50	50	50	55	55
Mean size of NbX[a] (nm)	40	55	55	60	65	65
Mean size of Laves phase[a] (nm)	–	200	200	200	245	200

[a] Volume fractions at 650 °C calculated by Thermo-Calc are 0.0194 for $M_{23}C_6$, 0.00226 for MX, and 0.0186 for Laves phase.

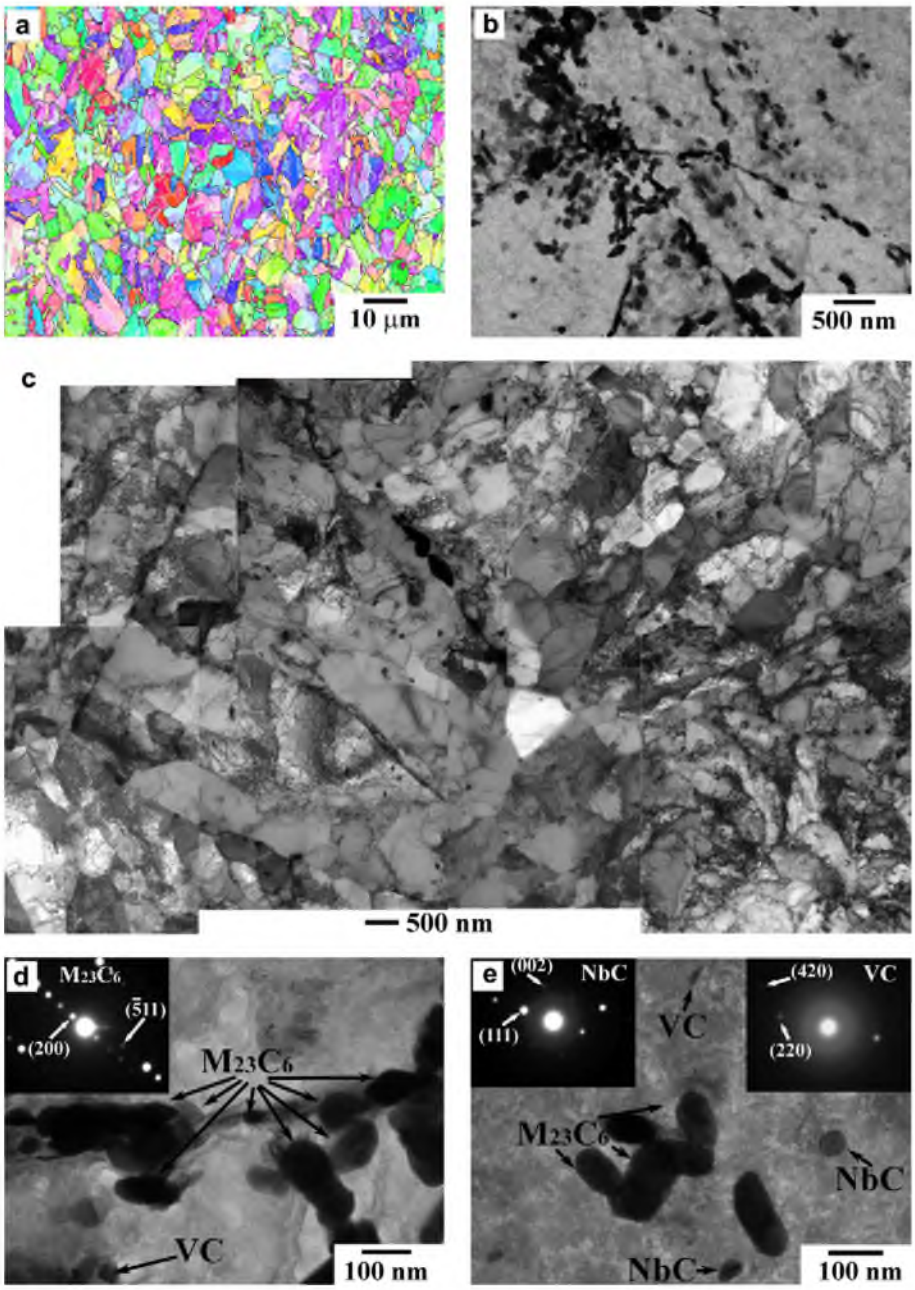

Fig. 1. Microstructure of a normalized steel tempered at 750 °C for 3 h: (a) OIM micrograph; (b–e) TEM micrographs of replica (b, d, and e) and foil (c). TEM micrographs (replica) show precipitation at a grain boundary (b and d) and at laths (b and e) and the corresponding electron diffraction patterns.

The minimal creep rate increases from approximately $10^{-8}\,s^{-1}$ to $10^{-6}\,s^{-1}$ when the nominal applied stress rises from 140 to 200 MPa. With increasing initial applied stress, the creep rate tends to increase, and the time to rupture tends to decrease. Three distinctive creep regimes with different strain dependence of the creep rate can be recognized in Fig. 2b. The creep rate rapidly decreases during transient creep, approaching its minimal value that is associated with steady state creep behavior. Finally, the creep rate increases until failure during accelerated (tertiary) creep.

It is worth noting that the changes in the creep behavior occur at certain creep strains, which do not depend greatly on the nominal creep stress. The transient creep corresponding to a decrease in the creep rate to a minimal value takes place at creep strains below approximately 1%. Subsequently, secondary creep, i.e., apparent steady-state flow, occurs at creep strains of up to approximately 4%. The tertiary creep regime leading to failure of the specimen takes place when the creep strain exceeds 5%. To study the crept microstructures corresponding to distinctly different creep regimes, several specimens were tested to different creep strains under an initial stress of 140 MPa. The creep strains that were selected for structural analysis are indicated by arrows in Fig. 2b.

3.3. Crept microstructures

The TMLS remains virtually unchanged in the grip portion of crept specimens during the test (Fig. 3). The transverse lath/subgrain sizes and the dislocation density within the interiors of laths/subgrains after prolonged aging at 650 °C for 1828 h and for the TMLS after tempering are almost the same (Table 1). By contrast, significant structural changes occur in the gauge section of the specimen. Typical crept microstructures that evolved at different strains are shown in Fig. 4. In general, microstructural

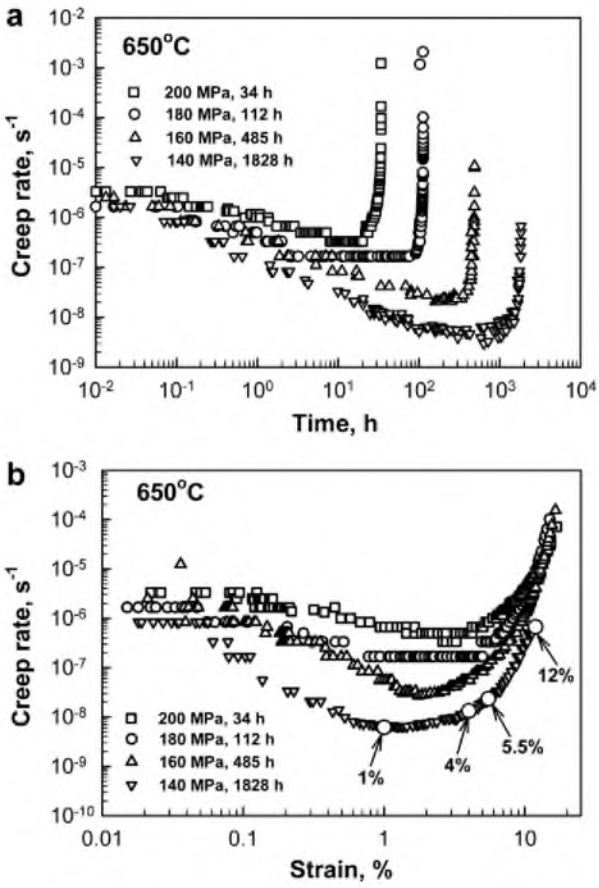

Fig. 2. Creep rate vs. time (a) and creep rate vs. strain (b) curves at 650 °C and different stresses of 140–200 MPa.

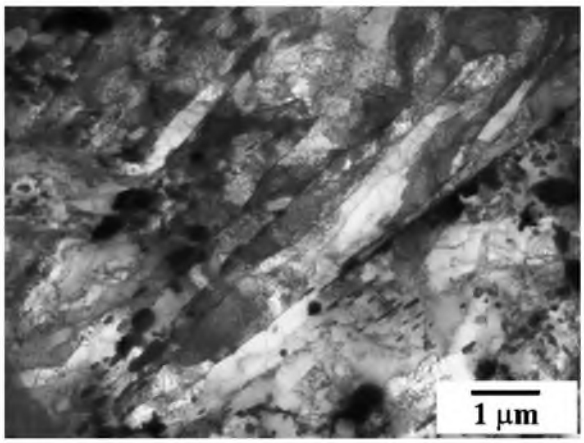

Fig. 3. TEM microstructure of steel at the grip portion of specimens after creep tests at 650 °C under a stress of 140 MPa for 1828 h.

evolution during creep is characterized by a gradual transformation of laths to subgrains and the continuous growth of subgrains/laths. Upon a creep test for 1828 h, the transverse lath and subgrain sizes increase to approximately 0.8 and 1.4 μm, respectively, which are 2–3 times larger than those in the tempered state (Table 1). Note here that the fraction of subgrains increases at the expense of the lath portions. In other words, the TMLS is progressively replaced by a subgrain structure during creep. The subgrain/lath growth is accompanied by a release of internal dislocations. The dislocation density after creep rupture is an order of magnitude lower than that in the tempered state (Table 1). Notably, grain growth is unimportant for the evolution of the TMLS; the grain size increases slightly to 3.6 μm during a creep test for 1828 h (Table 1).

In addition, the coarsening of second phase particles takes place. It is obvious that the grain/lath/subgrain growth takes place concurrently with particle coarsening (Table 1). It is observed in Fig. 5 that the size of $M_{23}C_6$-type carbides increases by a factor of almost

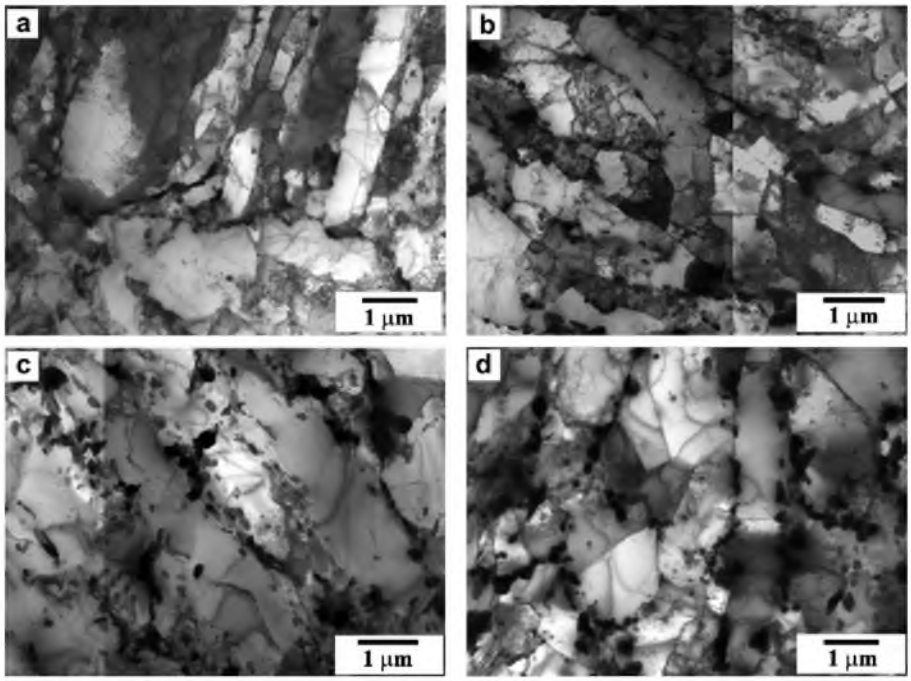

Fig. 4. TEM microstructure of steel in the gauge section of specimens after creep tests at 650 °C under a stress of 140 MPa to different strains: (a) 1%; (b) 4%; (c) 5.5%; (d) ruptured (12%).

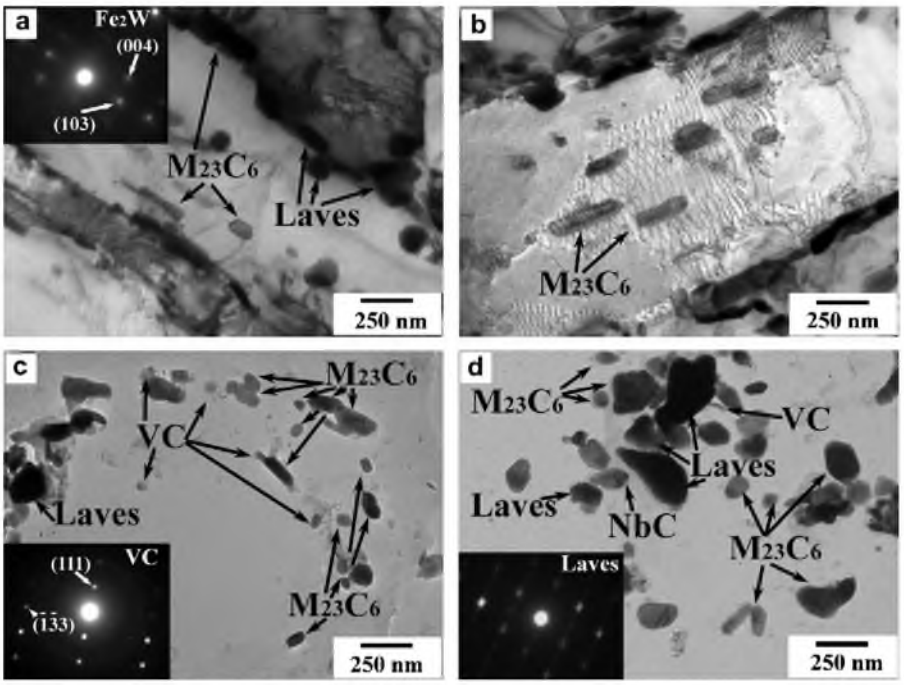

Fig. 5. TEM micrographs (a and b – foils; c and d – replica) show microstructure and precipitation at lath boundaries and corresponding electron diffraction patterns in the gauge sections of steel specimens after creep tests at 650 °C under a stress of 140 MPa: (a) 1%; (b and c) 5.5%, (d) 12%.

two up to 180 nm from the start of a creep test to failure. By contrast, the MX-type particles are relatively stable. The Nb-rich and V-rich M(C,N) carbonitrides demonstrate slow growth, and their average size is approximately 65 and 55 nm, respectively, in the neck portion of the fractured specimen (Fig. 5d). It should be noted that the coarsening of carbides/carbonitrides is accompanied by the appearance of rather large Laves phase particles, which precipitate in a heterogeneous manner on various boundaries (Fig. 6). Therefore, the experimental observation of Laves phase precipitation during creep does not support the hypothesis that at the initial creep stage, the fine Laves phase precipitates within the ferritic matrix provide additional precipitation strengthening, resulting in a decrease of the creep rate in the transient creep region [8]. It is obvious that Laves phase particles have a significant effect on the stabilization of the TMLS but their contribution to dispersion strengthening is virtually negligible. The mean size of Laves phase particles is 245 nm in the neck portion of the crept specimen. Because creep is accompanied by subgrain/lath growth, the moving boundaries leave some large particles in the subgrain/lath interior as clearly revealed by the Z-contrast technique (Figs. 6a and b).

The effect of creep strain on the size of various structural elements is quantitatively represented in Fig. 7. The variations of all structural parameters associated with the growth of laths/subgrains, the annihilation of interior dislocations, and the coarsening of second phase particles demonstrate almost the same strain dependencies. The laths/subgrains gradually grow during creep to a strain of 4%. On the other hand, the coarsening of $M_{23}C_6$ and MX particles is characterized by relatively fast kinetics under transient creep to a strain of 1%. Next, the sizes of the various particles become strain independent within the secondary creep regime in the strain range between 1% and 4%. There is evidence for an increasing growth rate for the subgrain/lath structure during incipient tertiary creep at strains of approximately 4–6% that is accompanied by significant coarsening of carbides, especially $M_{23}C_6$-type particles. The accelerated creep at strains above 6% is characterized by further growth of martensite laths and the coarsening of all secondary phases. The Laves phase and $M_{23}C_6$-type particles grow faster than the MX-type precipitates. It should be noted that the growth behavior of laths/subgrains clearly correlates with the decrease in the dislocation densities in the lath/subgrain interiors. The density of the $M_{23}C_6$ and Laves phase particles located at

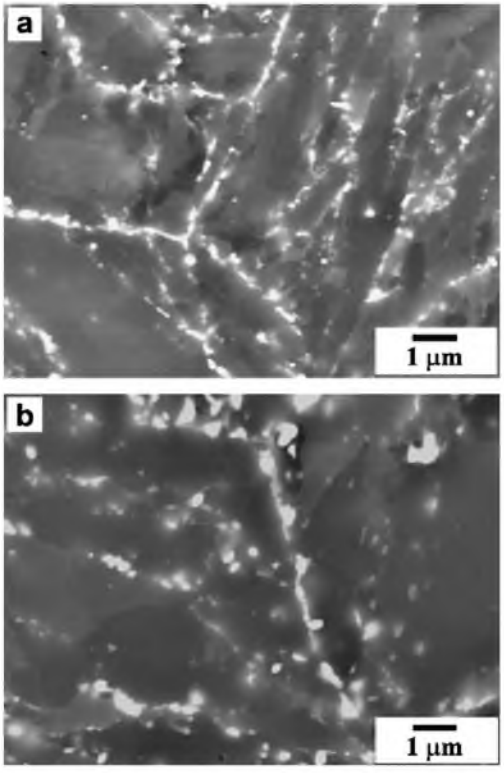

Fig. 6. SEM micrographs of the microstructure of steel in the gauge sections of specimens after creep tests at 650 °C under a stress 140 MPa to different strains: (a) 1%; (b) 12%.

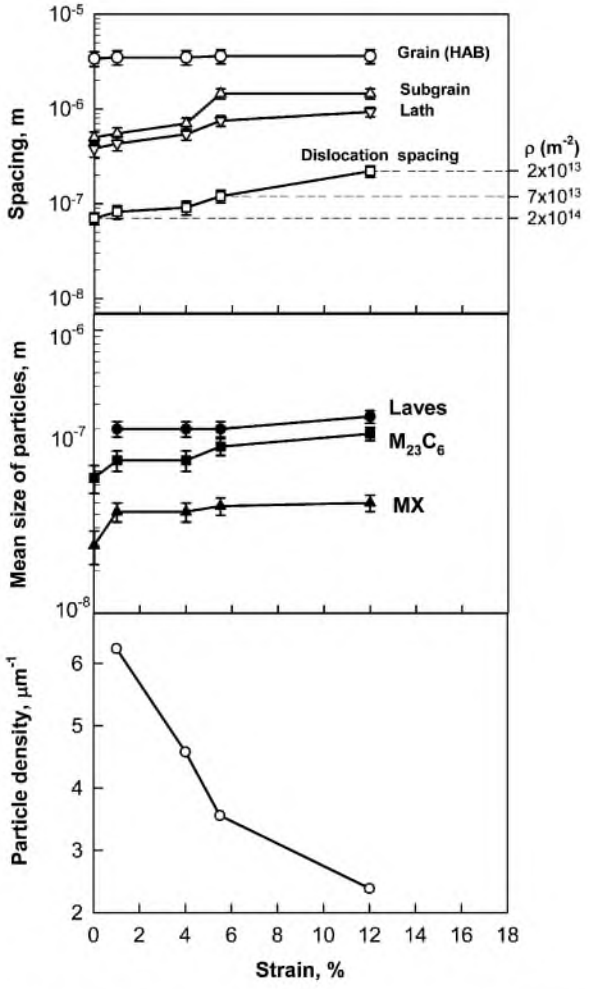

Fig. 7. Grain size, subgrain size, width of laths and inverse square root of dislocation density inside subgrains, mean size of particles and particle density at (sub)grain boundaries as function of strain in a steel during a creep test at 650 °C under a stress of 140 MPa.

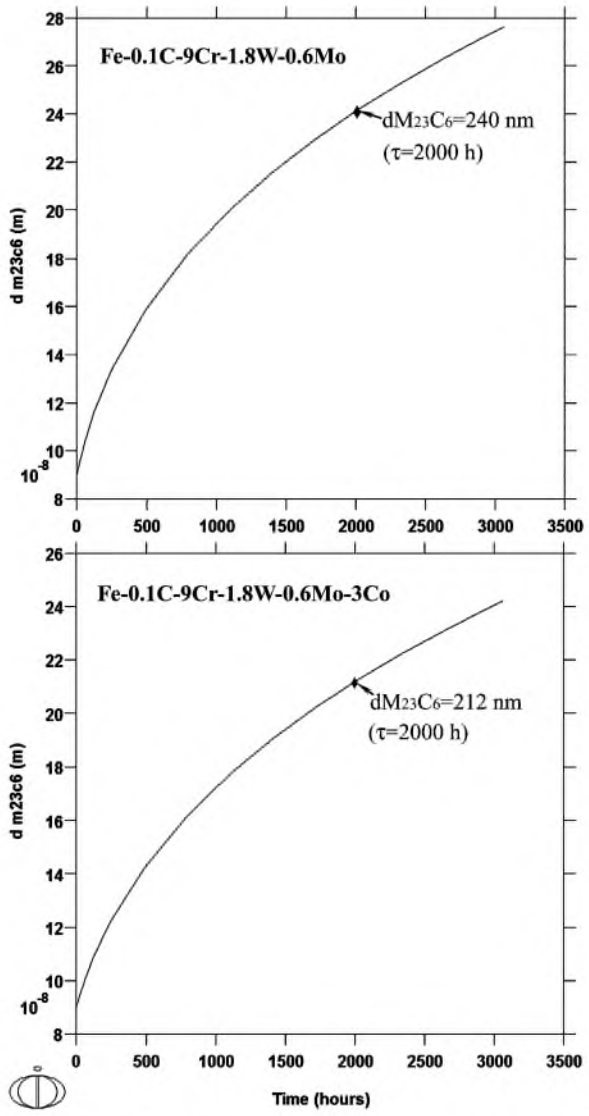

Fig. 8. Calculated temporal dependence of size of a $M_{23}C_6$ particle coarsening in Fe–0.1C–9Cr–1.8W–0.6Mo and Fe–0.1C–9Cr–1.8W–0.6Mo–3Co alloys at 650 °C. The initial particle size was 90 nm.

(sub)grain/lath boundaries was found to decrease with increasing creep strain (Fig. 7). This decrease is most pronounced in the strain range of approximately 4–6% during the transition to tertiary creep that is associated with an acceleration of subgrain/lath growth and particle coarsening. The mean values of the structural parameters for tempered and crept samples are summarized in Table 1.

4. Discussion

The creep behavior of the steel of interest is typical for heat resistant martensitic steels containing dispersed particles [1–3]. The creep rate decreases rapidly to its minimum at the early creep stage and then gradually increases with increasing creep strain. However, the present steel demonstrates improved creep resistance at 650 °C: the minimal creep rate for conventional P92 steel at 650 °C and 140 MPa was reported to be approximately 10^{-7} s^{-1} [29], whereas in the current study under the same creep conditions, the minimal creep rate amounts to less than 10^{-8} s^{-1} (Fig. 2). In addition, the present steel exhibits apparent steady-state flow in the strain range of 1% to 4%, while the P92 steel has a well-defined minimal creep rate; after reaching a minimum, the creep rate progressively increases until fracture [12,29]. This finding suggests that the alloying with Co extends the stage of steady-state flow in the P92 steel. Correspondingly, the rupture time for the present steel is approximately an order of magnitude higher than that for the P92 steel [12,23]. The effect of Co on the creep behavior may be associated with a stabilization of second phase precipitates [26], which in turn should provide an effective stabilization of grain/subgrain/lath boundaries and lattice dislocation density, leading to improved creep resistance. In particular, cobalt significantly affects the coarsening of $M_{23}C_6$ carbides during creep. Fig. 8 depicts the calculated results of the coarsening of a $M_{23}C_6$ carbide particle in the model Fe–0.1C–9Cr–1.8W–0.6Mo (all in wt%) alloys with and without cobalt at 650 °C. The initial size of the particle was assumed to be 90 nm. It is apparent that the size of the coarsened $M_{23}C_6$ particle after 2000 h is remarkably smaller in the alloy with 3 wt% Co (d = 212 nm) than in the alloy without cobalt (d = 240 nm). The results of the calculations are corroborated by experimental observations: the size of $M_{23}C_6$ particles in the present steel was found to be less than that in the P92 steel [12] at all strains.

Let us consider the pinning of grain/subgrain boundaries by various second phase particles. The randomly distributed particles cause a so-called Zener pinning pressure P_Z on a boundary [30,31]:

$$P_Z = \frac{3\gamma F_v}{d} \quad (1)$$

where γ is the boundary surface energy per unit area, and F_v and d are volume fraction (as calculated by Thermo-Calc) and the size of dispersed particles, respectively. When the particles are located at the boundaries, the pinning pressure on a boundary P_B depends on the size ratio of particles and (sub)grains/laths [32] and can be evaluated as:

$$P_B = \frac{\gamma F_{vB} D}{d^2} \tag{2}$$

where D represents the size of structural elements, i.e., the grain/subgrain size or lath thickness. The volume fraction F_{vB} of the particles located at the boundaries can be estimated taking into account the determined/estimated particle density β at the boundaries (Fig. 7). Under the assumption that the (sub)boundaries form a three-dimensional cubic arrangement with the grain edge length D, the length of the boundary per cell on the surface is $2D$, and the number of particles per unit boundary area can be written as

$$N_s = \frac{2D \cdot \beta}{D^2} = \frac{2\beta}{D} \tag{3}$$

On the other hand, the number of particles intersecting a unit area of the boundary is [31]

$$N_s = \frac{6F_{vB}}{\pi d^2} \tag{4}$$

and hence from Eqs. (3) and (4)

$$F_{vB} = \frac{\pi d^2 \beta}{3D} \tag{5}$$

The particle density β shown in Fig. 7 is the density of all precipitates located at the boundaries, i.e., $\beta = \beta_{M_{23}C_6} + \beta_{Laves}$. Assuming that at a strain of 1%, all $M_{23}C_6$ and Laves phase particles are located at lath and subgrain boundaries, i.e., $F_{v_{M_{23}C_6}} = F_{vB_{M_{23}C_6}}$ and $F_{v_{Laves}} = F_{vB_{Laves}}$, the density ratio of $M_{23}C_6$ and Laves phase particles on boundaries can be evaluated with their corresponding volume fractions and sizes $d_{M_{23}C_6}$ and d_{Laves}

$$\frac{\beta_{Laves}}{\beta_{M_{23}C_6}} = \frac{F_{vB_{Laves}} d^2_{M_{23}C_6}}{F_{vB_{M_{23}C_6}} d^2_{Laves}} \tag{6}$$

Then, the volume fractions F_{vB} of the $M_{23}C_6$ and Laves phase particles located at the boundaries at various creep strains can be calculated from the following relationship

$$\frac{F_{vB_i}}{F_{vB_0}} = \frac{D_0}{D_i} \cdot \frac{\beta_i}{\beta_0} \cdot \frac{d_i^2}{d_0^2} \tag{7}$$

where F_{vB_0}, D_0, β_0, and d_0 are the parameters for the $M_{23}C_6$ or/and Laves phase particles at a 1% strain, and F_{vB_i}, D_i, β_i, and d_i are the parameters at different creep strains.

Fig. 9 displays the pinning pressures on subgrain/lath boundaries from different types of second phase particles. The pinning pressures P_Z originating from homogeneously distributed particles on various boundaries were calculated using Eq. (1). Eq. (2) was used to calculate the pinning pressures P_B exerted by $M_{23}C_6$ and Laves phase particles, which are located at the boundaries. At a relatively small strain of 1%, the maximal pinning pressure is provided by $M_{23}C_6$ carbides located at the boundaries. Then, the pinning pressure P_B exerted by these particles gradually decreases with increasing creep strain (Fig. 9). Apparently, the observed gradual increase of the lath/subgrain size during creep is associated with stress-induced migration of the corresponding boundaries [33–35], which is accompanied by a detachment of boundaries from boundary precipitates. Therefore, the degradation of the pinning force exerted by the $M_{23}C_6$-type boundary precipitates results from a gradual decrease in the fraction of particles

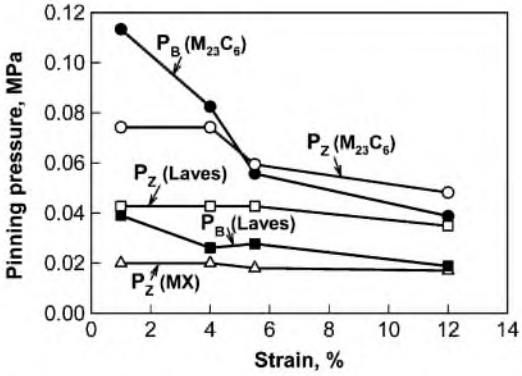

Fig. 9. Change of pinning pressures from different particles on grain and lath boundaries of steel during creep tests at 650 °C under a stress of 140 MPa.

located on the boundaries. At strains above 4%, the pinning pressure P_B from the boundary $M_{23}C_6$-precipitates becomes almost the same as the pressure P_Z that is evaluated under the assumption of a random particle distribution (Eq. (1)). The Laves phase appears as large particles; the particle size is comparable with the subgrain size even at a relatively small strain of 1%. Hence, the pinning pressures P_B and P_Z caused by these particles at a strain of 1% are the same. The decrease in the Laves phase particle density at the boundaries with increasing creep strain apparently diminishes the P_B pressure evaluated by Eq. (2), suggesting that the pinning pressure from Laves phases can be adequately predicted by Eq. (1). It is worth noting that the pinning pressures related to the MX-type precipitates are remarkably smaller than those from Laves phase particles, especially $M_{23}C_6$-type particles (Fig. 9).

The obtained results reveal that numerous second phase particles effectively stabilize the TMLS against static (sub)grain/lath growth. The TMLS is highly stable during long-term aging (in the grip portion of the specimens), i.e., the pinning pressure is high enough to stabilize the TMLS under static conditions. The subgrain/lath growth occurs only in the gauge sections of the crept specimens. Therefore, it can be concluded that this growth and the decrease of dislocation density are caused by plastic deformation.

An inspection of the pinning pressures shows that the $M_{23}C_6$-type carbides play a major role in the stabilization of the TMLS, and therefore, an increase of their resistance against Ostwald ripening is extremely important to increase the creep resistance of high chromium martensitic steels by additional alloying. The extension of the secondary creep stage in the present steel may be associated with an improved stability of $M_{23}C_6$-type carbides that seems to be affected by the addition of Co. Numerous boundary precipitates fix the TMLS under conditions of static aging and remarkably slow down the microstructure evolution during creep. The degradation of creep resistance and the acceleration of creep rate at strains of 4–5% are associated with a detachment of boundaries from pinning particles. Despite constant particle size, the strain range between 1% and 4% is characterized by a gradual increase in subgrain size. This increase suggests that the effect of the dispersed particles on the motion of lath and subgrain boundaries during plastic deformation is somewhat different from that considered under static conditions. The stress/strain-induced migration of dislocation boundaries leads to a deterioration of the acting pinning pressure from $M_{23}C_6$-type carbides; many of these particles appear within the interiors of subgrains, losing their efficiency for boundary pinning. As a result, the pinning pressure exerted by $M_{23}C_6$-type particles originally located at the boundaries decreases rapidly at strains above 4% leading to the accelerated creep.

5. Conclusions

The microstructures of a 3 wt% Co modified P92-type steel tempered and crept at 650 °C were studied. The main results can be summarized as follows.

1. After tempering at 750 °C for 3 h, the steel structure consisted of two substructural components including martensite laths with an average thickness of 380 nm and equiaxed subgrains having a size of approximately 500 nm. Numerous particles precipitated during the tempering treatment. $M_{23}C_6$-type particles with an average size of 90 nm precipitated on various interfaces including subgrain and lath boundaries. MX-type particles, i.e., VC and NbC with sizes of 20 and 40 nm, respectively, precipitated homogeneously throughout the martensite matrix.
2. The 3%Co modified P92 steel demonstrated superior creep resistance at 650 °C. The creep behavior of the studied steel was characterized by a more than tenfold reduced minimal creep rate and therefore a significantly increased creep rupture time compared to conventional P92 steel.
3. The structural changes during creep were associated with a gradual growth of martensite laths and subgrains. The mean sizes of laths and subgrains were 0.93 and 1.45 μm, respectively, in the specimen crept to failure, which occurred after 1828 h.
4. The lath/subgrain growth during creep was accompanied by a coarsening of $M_{23}C_6$ and MX-type particles that took place along with the precipitation of a relatively coarse Laves phase. The mean precipitate sizes in the neck portion of a specimen crept for 1828 h were found to be 185 nm for $M_{23}C_6$, 55 nm for VX, 65 nm for NbX, and 245 nm for Laves phase particles.
5. The $M_{23}C_6$-type carbides played a major role in the stabilization of the tempered martensite lath structure. The pinning pressure exerted by these particles was approximately two and four times higher than the pressures from Laves phase and MX-type particles, respectively, during creep to approximately 4%. The transition to tertiary creep correlated with a coarsening of the carbides and a detachment of lath and subgrain boundaries from chains of $M_{23}C_6$ carbides due to their strain-induced migration that led to a decreased pinning force from these particles.

Acknowledgements

This study was supported by the Ministry of Education and Science, Russia, under grant No. 02.740.11.5050. The authors are grateful to Dr. V. Skorobogatyh and Dr. I. Schenkova, Central Research Institute for Machine-Building Technology, for supplying the test material; to Prof. A. Solonin, National University of Science and Technology "MISIS", for Thermo-Calc calculations; and to the staff of the Joint Research Center, Belgorod State University, for their assistance with instrumental analysis.

References

[1] F. Abe, V. Taneike, K. Sawada, Int. J. Press. Vess. Pip. 84 (2007) 3–12.
[2] K. Kimura, Y. Toda, H. Kushima, K. Sawada, Int. J. Press. Vess. Pip. 87 (2010) 282–288.
[3] F. Abe, T. Horiuchi, M. Taneike, K. Sawada, Mater. Sci. Eng. A 378 (2004) 299–303.
[4] B. Sonderegger, S. Mitsche, H. Cerjak, Mater. Charact. 58 (2007) 874–882.
[5] R. Agamennone, W. Blum, C. Gupta, J.K. Chakravartty, Acta Mater. 54 (2006) 3003–3014.
[6] D. Rojasa, J. Garciab, O. Prata, L. Agudoc, C. Carrascod, G. Sauthoff, A.R. Kaysser-Pyzalla, Mater. Sci. Eng. A 528 (2011) 1372–1381.
[7] A. Kipelova, R. Kaibyshev, A. Belyakov, D. Molodov, Mater. Sci. Eng. A 528 (2011) 1280–1286.
[8] F. Abe, Metall. Mater. Trans. 36A (2005) 321–331.
[9] Q. Li, Metall. Mater. Trans. 37A (2006) 89–97.
[10] A. Kostka, K.-G. Tak, R.J. Hellmig, Y. Estrin, G. Eggeler, Acta Mater. 55 (2007) 539–550.
[11] J. Pesicka, R. Kuzel, A. Dronhofer, G. Eggeler, Acta Mater. 51 (2003) 4847–4862.
[12] V. Dudko, A. Belyakov, D. Molodov, R. Kaibyshev, Metall. Mater. Trans. A (2012), doi:10.1007/s11661-011-0899-1.
[13] F. Abe, Mater. Sci. Eng. A 387–389 (2004) 565–569.
[14] A. Aghajani, Ch. Somsen, G. Eggeler, Acta Mater. 57 (2009) 5093–5106.
[15] H.Gh. Armaki, R. Chen, K. Maruyama, M. Igarashi, Metall. Mater. Trans. A (2011), doi:10.1007/s11661-011-0726-8.
[16] A. Kabadwal, M. Tamura, K. Shinozuka, H. Esaka, Metall. Mater. Trans. 41A (2010) 364–379.
[17] M. Nakajima, S.-i. Komazaki, Y. Kohno, Int. J. Press. Vess. Pip. 86 (2009) 563–569.
[18] J. Hald, Int. J. Press. Vess. Pip. 85 (2008) 30–37.
[19] M. Taneike, K. Sawada, F. Abe, Metall. Mater. Trans. 35A (2004) 1255–1262.
[20] M. Taneike, F. Abe, K. Sawada, Nature 424 (2003) 294–296.
[21] K. Suzuki, S. Kumai, Y. Toda, H. Kushima, K. Kimura, ISIJ Int. 43 (2003) 1089–1094.
[22] A.Yu. Kipelova, A.N. Belyakov, V.N. Skorobogatykh, I.A. Shchenkova, R.O. Kaibyshev, Met. Sci. Heat Treat. 52 (2010) 100–110.
[23] F. Abe, Mater. Sci. Eng. A 510–511 (2009) 64–69.
[24] N. Dudova, R. Kaibyshev, ISIJ Int. 51 (2011) 826–831.
[25] T. Horiuchi, M. Igarashi, F. Abe, ISIJ Int. 42 (2002) S67–S71.
[26] L. Helis, Y. Toda, T. Hara, H. Miyazaki, F. Abe, Mater. Sci. Eng. A 510-511 (2009) 88–94.
[27] Y.F. Yin, R.G. Faulkner, Mater. Sci. Eng. A 344 (2003) 92–102.
[28] H. Kitahara, R. Ueji, N. Tsuji, Y. Minamino, Acta Mater. 54 (2006) 1279–1288.
[29] K. Kimura, K. Sawada, H. Kushima, K. Kubo, Int. J. Mater. Res. 99 (2008) 395–401.
[30] C.S. Smith, Trans. AIME 175 (1948) 15–51.
[31] F.J. Humphreys, M. Hatherly, Recrystallization and Related Annealing Phenomena, Pergamon Press, UK, 1996.
[32] W.B. Hutchinson, B.J. Duggan, Met. Sci. 12 (1978) 372–380.
[33] D.A. Molodov, V.A. Ivanov, G. Gottstein, Acta Mater. 55 (2007) 1843–1848.
[34] T. Gorkaya, D.A. Molodov, G. Gottstein, Acta Mater. 57 (2009) 5396–5405.
[35] D.A. Molodov, T. Gorkaya, G. Gottstein, J. Mater. Sci. 46 (2011) 4318–4326.